



Provided by the author(s) and University of Galway in accordance with publisher policies. Please cite the published version when available.

| | |
|-----------------------------|---|
| Title | A dislocation-based yield strength determination model in nano-indentation test |
| Author(s) | Tao, Ping; Ye, Fei; Gong, Jianming; Barrett, Richard A.; Leen, Sean B. |
| Publication Date | 2021-02-20 |
| Publication Information | Tao, Ping, Ye, Fei, Gong, Jianming, Barrett, Richard A., & Leen, Seán B. (2021). A dislocation-based yield strength model for nano-indentation size effect. <i>Proceedings of the Institution of Mechanical Engineers, Part L: Journal of Materials: Design and Applications</i> . doi:10.1177/1464420721992796 |
| Publisher | SAGE Publications |
| Link to publisher's version | https://doi.org/10.1177/1464420721992796 |
| Item record | http://hdl.handle.net/10379/16668 |
| DOI | http://dx.doi.org/10.1177/1464420721992796 |

Downloaded 2024-04-19T18:08:05Z

Some rights reserved. For more information, please see the item record link above.



1 **A dislocation-based yield strength model for nano-indentation size effect**

2 Ping Tao^{1,2,4}, Fei Ye^{1,2}, Jianming Gong^{1,2}, Richard A. Barrett^{3,4}, Seán B. Leen^{3,4}

3 ¹School of Mechanical and Power Engineering, Nanjing Tech University, China;

4 ²Jiangsu Key Lab of Design and Manufacture of Extreme Pressure Equipment, China;

5 ³I-Form Advanced Manufacturing Research Centre, Ireland;

6 ⁴Mechanical Engineering, School of Engineering, College of Science and Engineering,
7 National University of Ireland Galway, Ireland.

8 **Abstract**

9 This paper presents a dislocation-based yield strength model for the nano-indentation
10 size effect. The model is based on functional expressions involving the densities of
11 statistically stored dislocations (SSDs) and geometrically necessary dislocations (GNDs).
12 A single-phase austenitic stainless steel (316L) and a ferrite-austenite dual-phase steel
13 (2205) are used here as the case-study materials to validate the proposed model.
14 Experimental testing and finite element modelling (FEM) of nano-indentation of the two
15 materials are presented. Experimental tests are performed in the indentation load range
16 from 1000 μN to 10000 μN . For 2205 steel, FEM is performed using a dual-phase
17 microstructure-based model. It is shown that, with consideration of SSDs and GNDs, FEM
18 results can reproduce measured load-displacement curves and hence, the size effect, within
19 an error range of about 5%.

20

21 **Keywords:** Nano-indentation; yield strength; dislocation; finite element model;
22 indentation size effect

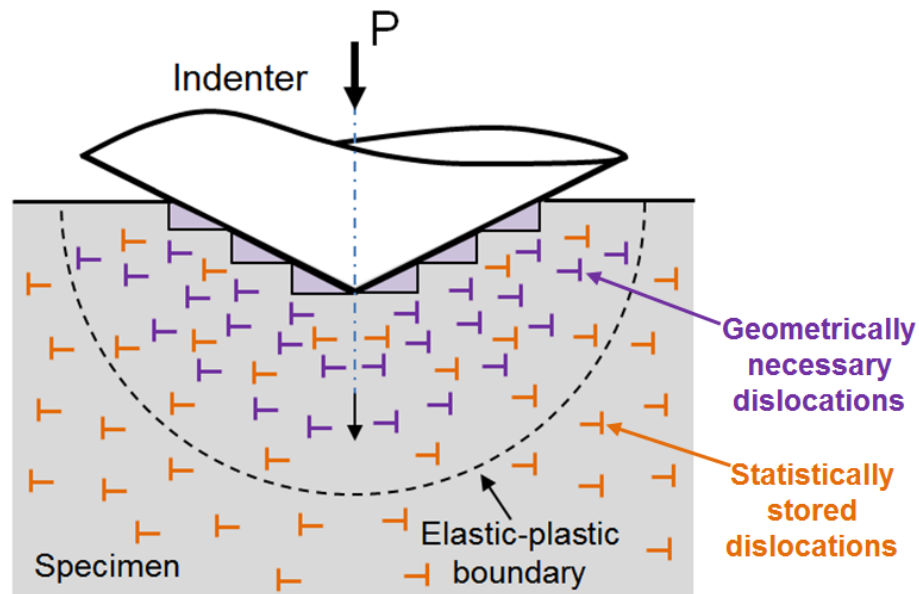
23 1. Introduction

24 Nano-indentation (NI) has been extensively performed to characterize and extract the
25 mechanical properties of materials at small length-scales, especially for investigations of
26 local micro-scale regions or phases. Due to the shallow depth of the test, NI is considered
27 as a non-invasive and non-destructive method that is useful for condition monitoring of
28 materials and structures utilized in severe environments (e.g. nuclear reactor and plant). In
29 a continuous and timely manner, the environment induced damage can be characterized
30 from the variation of material properties.

31 It has been found that a large number of factors can affect the nanoindentation testing
32 results, e.g. indentation size effect [1, 2, 3, 4] , creep phenomenon [5, 6], substrate
33 effects [7] and uniqueness problem [8, 9]. For metallic systems, the indentation size effect
34 (ISE) is considered to be the most significant factor. While the research on the other factors
35 mentioned is limited, most are related to specific testing conditions. For example, the
36 substrate effect is specific to the characteristics of the coating or composite material, the
37 indentation creep phenomenon is primarily an issue at very low testing rates. The
38 uniqueness problem is only relevant to dimensionless inverse analysis methods, which are
39 not used here. The focus of this paper is the size effect (ISE), a phenomenon whereby nano-
40 hardness, for example, increases with decreasing indentation depth. Dislocation-based
41 mechanisms have been used to explain the ISE phenomenon. Based on strain gradient
42 plasticity theory [10, 11], dislocations in metallic materials are generally divided into two
43 types: (i) statistically stored dislocations (SSDs) and (ii) geometrically necessary
44 dislocations (GNDs). SSDs refer to dislocations caused by mutual trapping in a random
45 way, whilst GNDs are dislocations that eliminate incompatibility of plastic deformation
46 caused by non-uniform dislocation slip within a polycrystal [12]. As shown schematically
47 in **Fig. 1**, during the NI test, GNDs are more concentrated near the indenter in the plastic
48 regions, showing a higher dislocation density due to the higher strain gradient. However,
49 SSDs are more uniformly distributed in the specimen, independent of depth. The total

50 density of dislocations represents coupling between SSDs and GNDs, resulting in the
51 combined effects on hardening in materials [13]. In order to demonstrate the identified
52 mechanical properties taking into account dislocation effects and to improve analytical
53 functions for extraction of mechanical properties from experimental data, complementary
54 finite element modeling (FEM) of the indentation process is presented.

55



56

57 **Fig. 1.** Schematic diagram of the distribution of geometrically necessary dislocations
58 and statistically stored dislocations generated by an axisymmetric conical indenter.

59

60 Based on identified parameters by NI tests [14, 15, 16], power-law hardening can
61 describe the overall elasto-plastic behavior of steels. In addition to Young's modulus and
62 hardness, other mechanical properties (such as yield strength and hardening exponent) are
63 also required. In order to comprehensively describe the full range of macroscopic stress-
64 strain curves, many attempts have been made to develop an efficient and convenient
65 method to extract macro-scale mechanical properties from NI tests. When using these
66 determined macro-scale parameters in FEM to reproduce the indentation load-
67 displacement curves at the micro-scale, large differences can be found in the comparisons

68 between simulation results and experimental tests. This study presents a quantitative yield
69 strength determination model applied for NI testing at variable micro-scale indentation
70 depths. In order to differentiate from the more commonly-used definition of yield strength,
71 the NI-determined values are often referred as the representative yield strength [16, 17].
72 The aim of this work is to rationalize the indentation size effect and reduce the modeling
73 errors compared with experimental data. In order to validate the proposed model,
74 experimental tests were performed using both single-phase (316L stainless steel, SS) and
75 dual-phase (2205 duplex stainless steel, DSS) materials. FEM of the single- and dual-phase
76 materials was also employed using the proposed dislocation-based model for comparison
77 purposes.

78

79 **2. Model framework**

80 **2.1. Analytical description**

81 As mentioned above, SSDs and GNDs are regarded as the two dominant factors in
82 contribution to hardening performance of materials during deformation. Based on the
83 **Taylor** hardening theory [18, 19], the representative yield strength (σ_y^R) coupled in a linear
84 form by SSDs (σ_y^{SSD}) and GNDs (σ_y^{GND}) can be defined as [12]:

$$\sigma_y^{SSD} = M\alpha Gb\sqrt{\rho_{SSD}} \quad , \quad \sigma_y^{GND} = M\alpha Gb\sqrt{\rho_{GND}} \quad (1)$$

$$\sigma_y^R = \sigma_y^{SSD} + \sigma_y^{GND} \quad (2)$$

85 where M is the Taylor factor; α is a material constant, called Taylor coefficient; G is
86 the shear modulus, $G = E/2(1 + \nu)$, E is the elastic modulus, ν is the Poisson's ratio;
87 b is the Burgers vector; ρ_{SSD} is the density of statistically stored dislocations and ρ_{GND}
88 is the density of geometrically necessary dislocations.

89 According to the description by **Nix and Gao** [20], the density of GNDs generated in

90 the NI test using a conical indenter is as follows:

$$\rho_{\text{GND}} = \frac{3}{2bh} \tan^2 \theta \quad (3)$$

91 where h is the displacement; θ is the angle of the cone made within the specimen free
 92 surface; for a Berkovich indenter, $\tan \theta = 0.358$.

93 For SSDs, it is considered that the intrinsic hardness (H_0) arises from SSDs alone,
 94 which is independent of indentation depth. On this basis, the density of SSDs can be
 95 described as [12]:

$$\rho_{\text{SSD}} = \left(\frac{H_0}{\kappa M \alpha G b} \right)^2 \quad (4)$$

96 Combining **Eqs. (1-4)**, the representative yield strength as a function of indentation
 97 depth can be expressed as:

$$\sigma_y^R = \frac{H_0}{\kappa} + M \alpha G b \sqrt{\frac{3}{2bh} \tan^2 \theta} \quad (5)$$

98 where H_0 is the hardness independent of indentation depth; κ is the Tabor factor. At a
 99 small depth range of 50 nm and 3000 nm, the value of κ is determined as 4.15 by
 100 **Gutierrez et al.** [2]. The related physical constants of ferrite and austenite adopted from
 101 the body-centered cubic (BCC) structure and face-centered cubic (FCC) structure,
 102 independent of NI tests, are listed in **Table 1**.

103

104

Table 1. Physical constants of ferrite and austenite.

| Parameter | Ferrite (BCC) | Austenite (FCC) | Source |
|-----------|---------------|-----------------|----------|
| M | 2.9 | 3.06 | [18, 19] |
| α | 0.23 | 0.23 | [18, 19] |
| b (nm) | 0.2482 | 0.2503 | [18, 19] |

105

106 2.2. Finite element model

107 The analytical model described in the previous section is applied here to simulate the

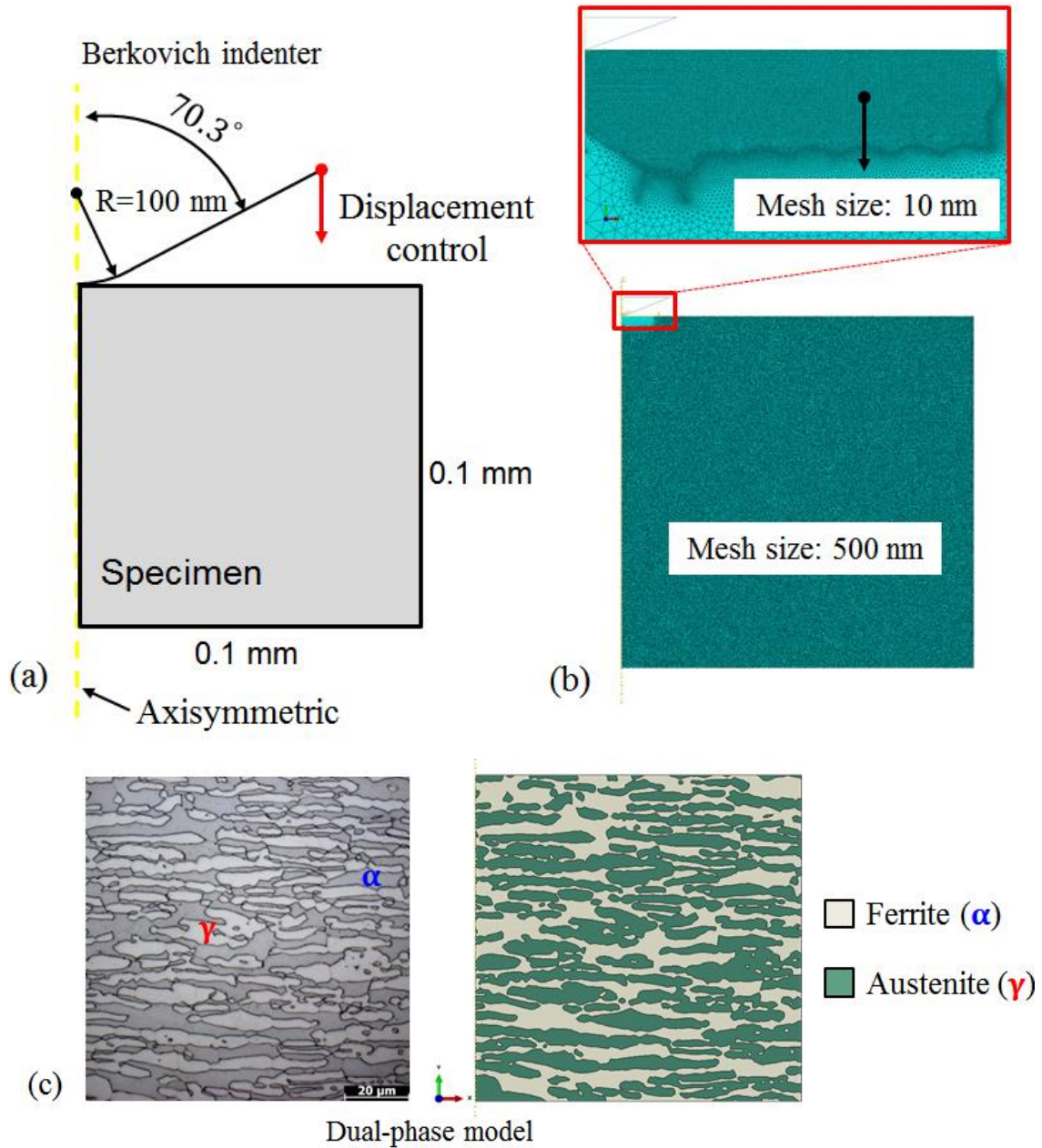
108 NI tests. An axisymmetric two-dimensional (2D) finite element model with a size of
109 $0.1 \text{ mm} \times 0.1 \text{ mm}$ was built in Abaqus software, as shown in **Fig. 2**. In the 2D case,
110 the geometry of the Berkovich indenter was simplified to a conical indenter with a half-
111 cone-angle of 70.3° [21, 22]. As the elastic modulus of the Berkovich indenter is 1140
112 GPa, it was represented as a rigid body in the 2D axisymmetric model.

113 In order to save computational time and ensure sufficient computational accuracy, the
114 mesh of a local contact region between indenter and specimen was refined to triangle
115 element size of 10 nm, with a coarse mesh size of size 500 nm away from the indentation
116 contact region, as shown in **Fig. 2b**. In addition, adaptive re-meshing was applied to
117 improve the quality of the simulation results. Sensitivity analyses were previously
118 performed to ensure that the mesh was sufficiently refined to achieve converged,
119 numerically stable and mesh-independent results. The FE model contains 458977 linear
120 triangular elements of type CAX3. A fixed boundary condition was applied at the bottom
121 surface of the model. The left surface is the symmetry axis and can only move vertically.

122 During the simulations, vertical displacement control is implemented to simulate
123 indentation and the contact between the indenter and specimen is defined to be frictionless,
124 for the base case. The resulting load-displacement response corresponds to the applied
125 axial displacement and associated (axial) reaction force on the indenter.

126 For DSS 2205, in order to represent the dual-phase structure, a representative optical
127 micrograph of size $0.1 \text{ mm} \times 0.1 \text{ mm}$ was vectorized and inserted into the FE model,
128 as presented in **Fig. 2c**. The embedded microstructure was obtained from the cross section,
129 which represented the ferrite-austenite structure along the depth direction during the
130 indentation process.

131



132

133

134

135

136

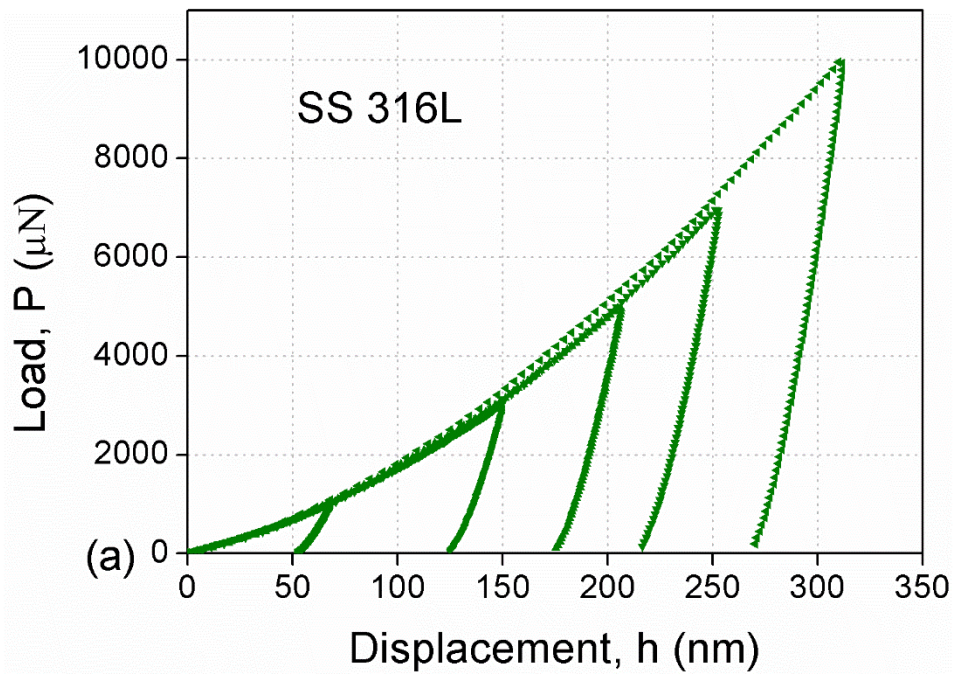
137

Fig. 2. (a) Overall view of the axisymmetric finite element model with a simplified 2D Berkovich indenter, tip radius $R=100\text{ nm}$; (b) local view of the refined mesh region and (c) dual-phase microstructure-based model for 2205 duplex stainless steel.

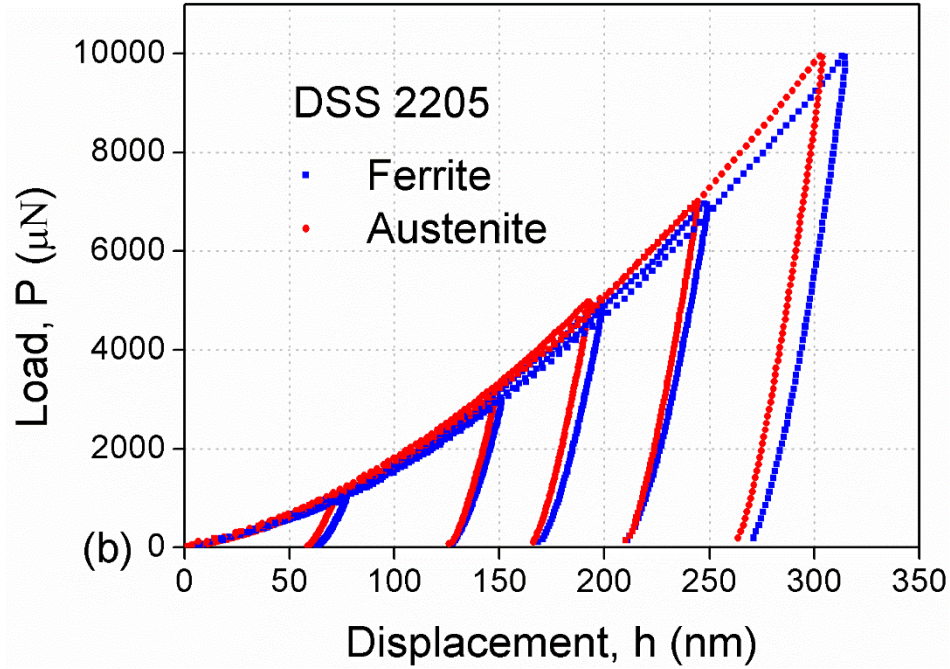
138 **3. Results and discussion**

139 NI tests were carried out on Bruker's Hysitron TI-Premier instrument with a standard
140 diamond Berkovich indenter. Specimens were pre-ground to 2000 grit, and then followed
141 by mechanical and electro polishing procedures to ensure a low roughness sample surface
142 for testing. After sample polishing preparation, the ferrite and austenite can be identified
143 in-situ using microscopy, during testing, as shown in Fig. 2c, with ferrite in light colour
144 and austenite in dark. Indentation tests were employed in the load range from 1000 μN to
145 10000 μN . The loading and unloading time was set to 5s to avoid room temperature creep
146 phenomenon under a low loading rate [5, 6]. For each load level test, at least five separate
147 areas were selected and five different indentation points were performed. The distance
148 between adjacent indentations was set to be 10 μm to eliminate the mutual influence of
149 indentation points. A group of obtained load-displacement curves of SS 316L and DSS
150 2205 under variable loads are presented in **Fig. 3**.

151



152



153

154

Fig. 3. Load-displacement curves of (a) SS 316L and (b) ferrite and austenite in DSS

155

2205 under the maximum indentation load varying from 1000 μN to 10000 μN .

156

157

According to the **Oliver-Pharr** methodology [23, 24], values of the nano-hardness

158

and reduced modulus are determined by **Eqs. (6-8)**:

$$H = \frac{P_{\max}}{A_c} \quad (6)$$

$$E_r = \frac{\sqrt{\pi}S}{2\sqrt{A_c}} \quad (7)$$

$$A_c = C_0 h_c^2 + C_1 h_c + C_2 h_c^{\frac{1}{2}} + C_3 h_c^{\frac{1}{4}} + C_4 h_c^{\frac{1}{8}} + C_5 h_c^{\frac{1}{16}} \quad (8)$$

159

where H is the nano-hardness; P_{\max} is the maximum load force; A_c is the contact area;

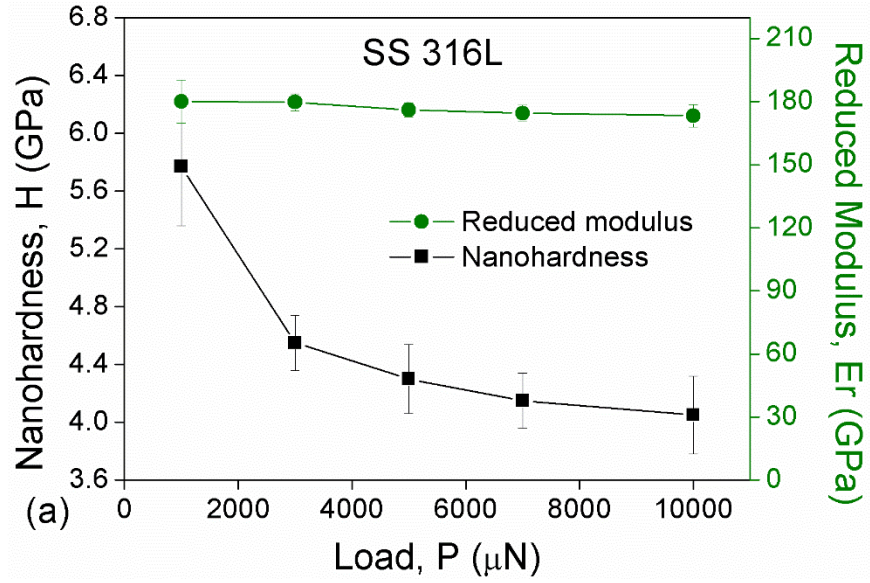
160

E_r is the reduced modulus; S is the contact stiffness of the initial unloading curve defined

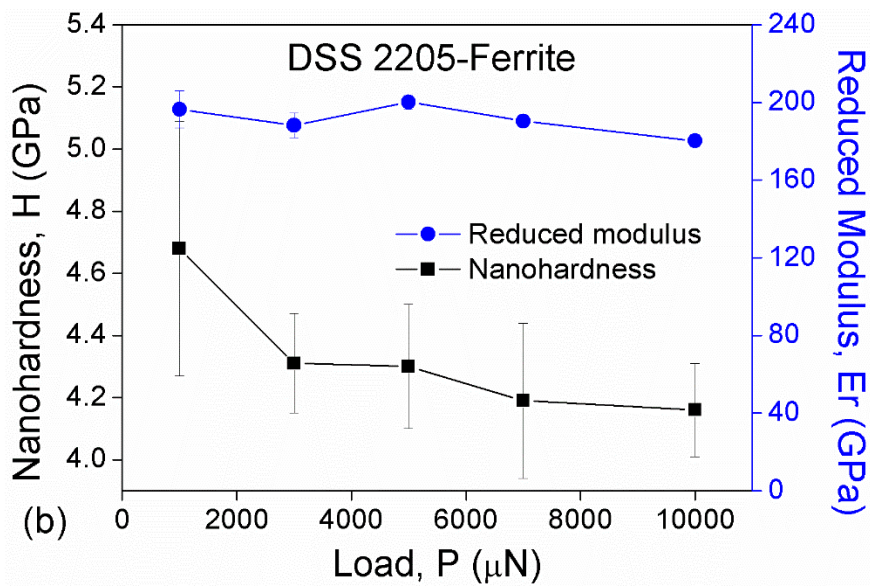
161

by dP/dh and h_c is the contact displacement.

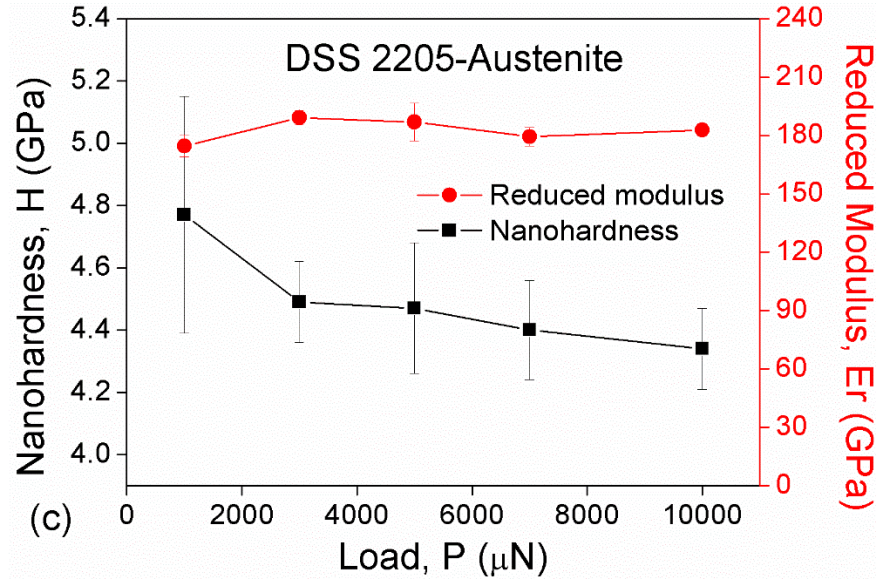
162



163



164



165

166 **Fig. 4.** The identified values of nano-hardness and reduced modulus of (a) SS 316L, (b-c)
 167 ferrite and austenite in DSS 2205.

168

169 The identified values of nano-hardness and reduced modulus of SS 316L and DSS
 170 2205 are plotted in **Fig. 4**. Young's modulus is determined from reduced modulus by the
 171 following expression:

$$\frac{1}{E_r} = \frac{1 - \nu^2}{E} + \frac{1 - \nu_i^2}{E_i} \quad (9)$$

172 where E is the elastic modulus; ν is the Poisson's ratio, set as a value of 0.3 for both
 173 316L and 2205; $E_i = 1140$ GPa and $\nu_i = 0.07$ are the elastic modulus and Poisson's
 174 ratio of the diamond Berkovich indenter, respectively. According to **Eq. (9)**, the average
 175 values of elastic modulus of SS 316L, ferrite and austenite in DSS 2205 determined here
 176 are 190.19 GPa, 208.61 GPa and 197.69 GPa, respectively.

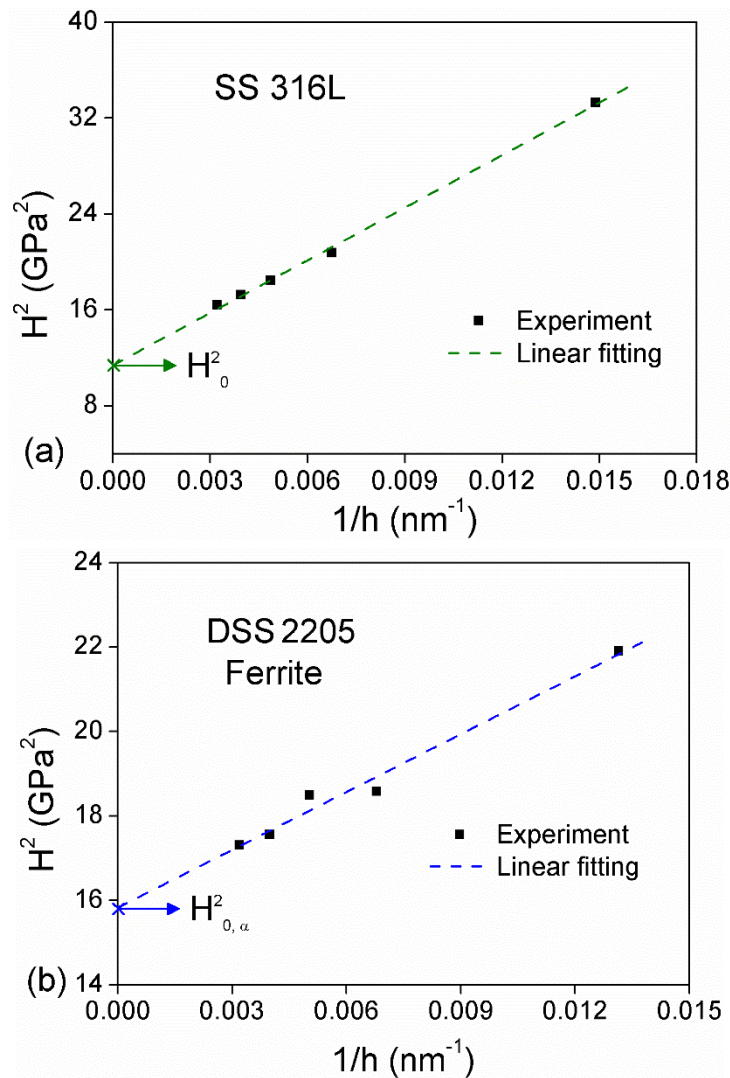
177 As shown in **Fig. 4**, the values of nano-hardness of both 316L and 2205 are dependent
 178 on testing load (i.e. indentation depth), consistent with the ISE phenomenon in previously
 179 published research [1, 2, 3]. The values of intrinsic hardness H_0 of 316L and 2205 are
 180 determined by the relationship between the nano-hardness determined by **Oliver-Pharr**

181 method [23, 24] and indentation displacement recorded in tests, expressed as [20]:

$$\left(\frac{H}{H_0}\right)^2 = 1 + \frac{h^*}{h} \quad (10)$$

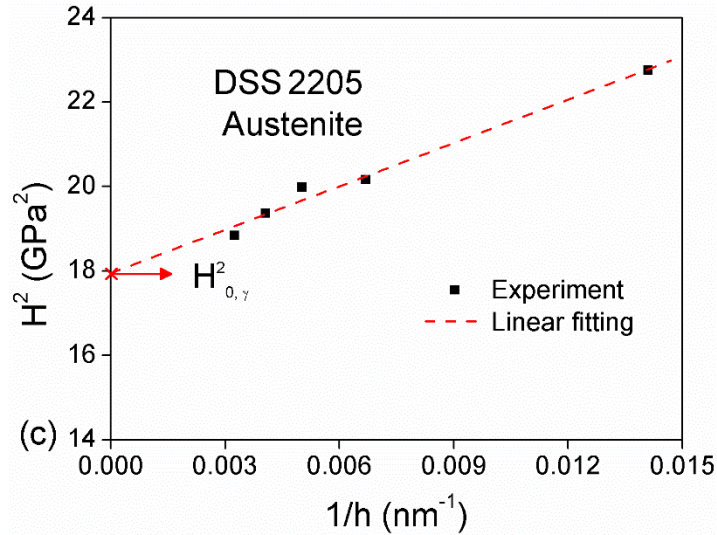
182 where H is the determined nano-hardness based on **Eq. (6)**; h is the maximum
183 displacement; h^* is a characteristic length. The values of H_0 and h^* are determined
184 based on a linear fitting between H^2 and $1/h$. As presented in **Fig. 5**, the intrinsic
185 hardness of SS 316L (H_0^{316L}), ferrite ($H_{0,\alpha}^{2205}$) and austenite ($H_{0,\gamma}^{2205}$) in DSS 2205 are
186 determined as 3.37 GPa, 3.97 GPa and 4.24 GPa, respectively.

187



188

189



190

191 **Fig. 5.** Linear fitting curves between H^2 and $1/h$ of (a) 316L, (b, c) ferrite and

192

austenite in DSS 2205.

193

194 Based on the above analyses, according to **Eq. (5)**, the representative yield strength
 195 of 316L and DSS 2205 (ferrite and austenite) under variable testing loads can be
 196 determined, as listed in **Table 2** and **Table 3**. It is shown that the values of yield strength
 197 decreases with the increase of load.

198

199

Table 2. Identified representative yield strength values of SS 316L.

| Load, P (μN) | Representative yield strength, σ_y^R (MPa) |
|--------------|---|
| 1000 | 2190.31 |
| 3000 | 1740.36 |
| 5000 | 1600.06 |
| 7000 | 1522.69 |
| 10000 | 1452.14 |

200

201

202

203 **Table 3.** Identified representative yield strength values of DSS 2205 (ferrite and
 204 austenite).

| Load, P (μN) | Representative yield strength, σ_y^R (MPa) | |
|--------------|---|-----------|
| | Ferrite | Austenite |
| 1000 | 2296.88 | 2415.71 |
| 3000 | 1907.64 | 1987.59 |
| 5000 | 1782.72 | 1862.50 |
| 7000 | 1694.79 | 1769.84 |
| 10000 | 1617.42 | 1691.21 |

205

206 The overall stress-strain curves of 316L and 2205 input in the finite element models
 207 are determined based on the power-law assumption [16, 17], described as:

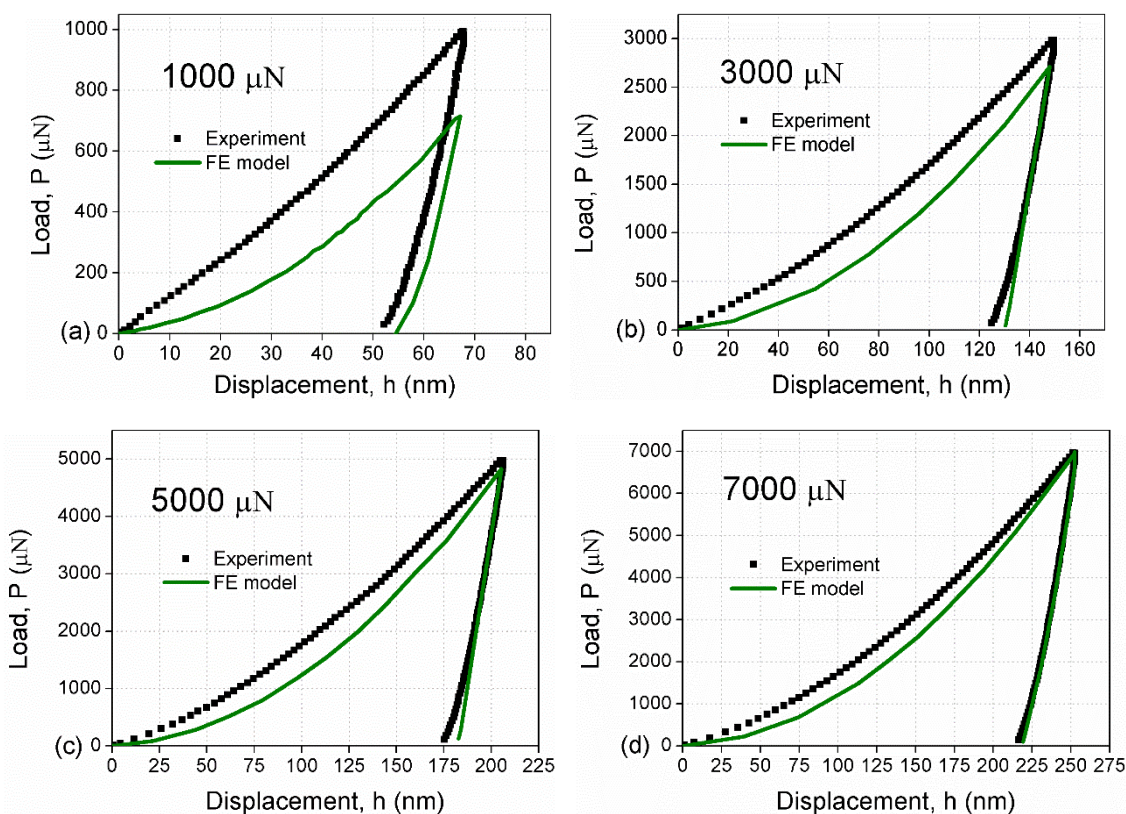
$$\sigma = \sigma_y^R \left(1 + \frac{E}{\sigma_y^R} \varepsilon_p \right)^n \quad (11)$$

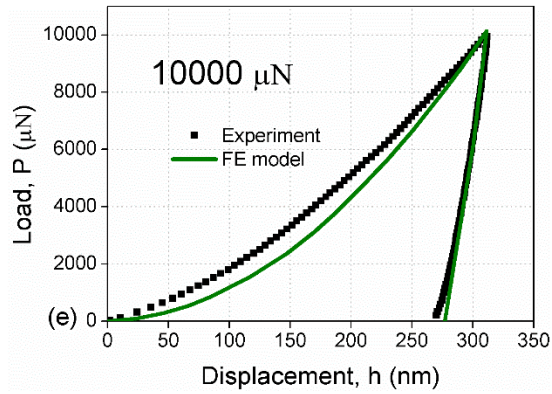
208 where σ_y^R is the identified representative yield strength, E is the elastic modulus, ε_p is
 209 the plastic strain and n is the hardening exponent. In this study, only the values of
 210 representative yield strength are considered to depend on indentation depth; the hardening
 211 exponent is assumed to be consistent with the macro-scale value. The value of hardening
 212 exponent of 316L is determined as 0.15 from a fitting analysis based on the true stress-
 213 strain curves from uniaxial tensile tests. The adopted values of hardening exponent of
 214 ferrite and austenite in DSS 2205 are 0.124 (ferrite) and 0.134 (austenite) from our previous
 215 nano-indentation study [25]. Combining **Eq. (5)** and **Eq. (11)**, the mechanical performance
 216 at different indentation depths can be determined and input as plasticity parameters in the
 217 FEM.

218 **Fig. 6** and **Fig. 7** present the comparisons of load-displacement curves of SS 316L
 219 and DSS 2205 between experimental tests and numerically predicted results. The errors of
 220 maximum load between experimental data and FE simulation results are listed in **Table 4**

221 and **Table 5**. It can be found that the numerically predicted results are in general close to
 222 the experimental data (with an error of about 5%) for the cases of indentation load from
 223 3000 μN to 10000 μN . The intuitive comparisons between FEM contour plots and
 224 experimental scanning residual morphologies of ferrite and austenite in DSS 2205 under
 225 5000 μN are also presented here in **Fig. 8**. It is shown that the model predicts a 4.83%
 226 larger plastic zone for the ferrite than austenite and the test indicates 5.64% larger for ferrite.
 227 This is an important and consistent prediction with respect to the differentiation of response
 228 between the two phases of the dual-phase steel [25, 26, 27]; specifically, in DSS 2205,
 229 the ferrite matrix exhibits a lower nano-hardness value than austenite, resulting in a lighter
 230 residual indentation morphology in the ferrite.

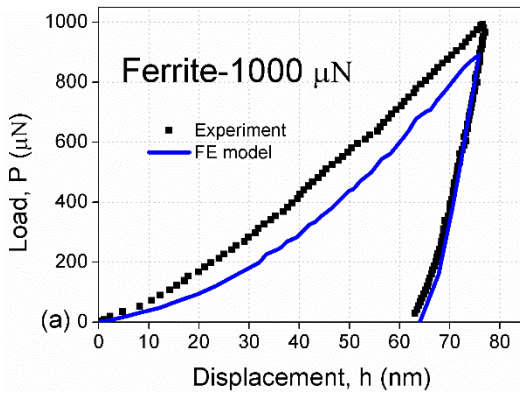
231



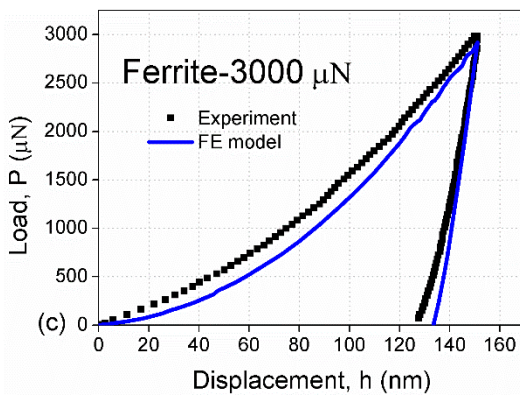
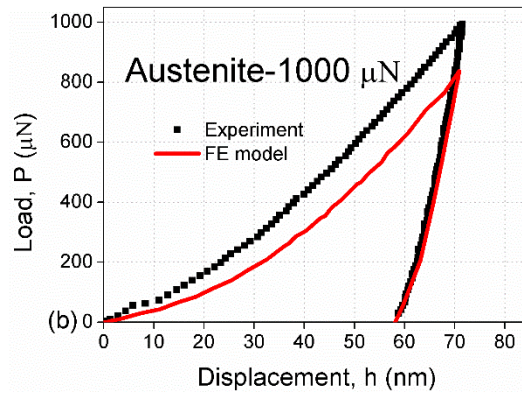


234

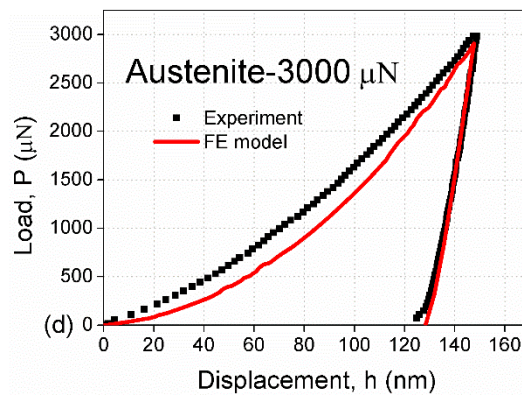
235 **Fig. 6.** Comparisons of load-displacement curves between experimental data and
 236 numerically predicted results of SS 316L.
 237

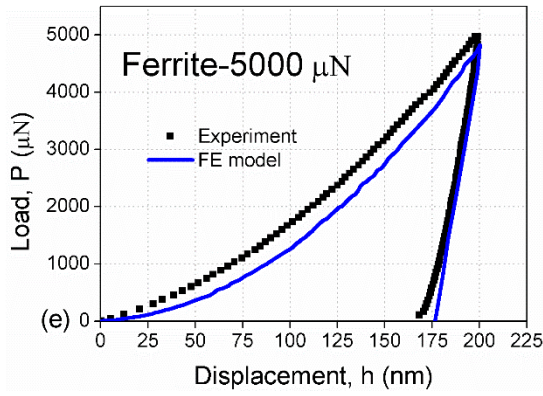


238

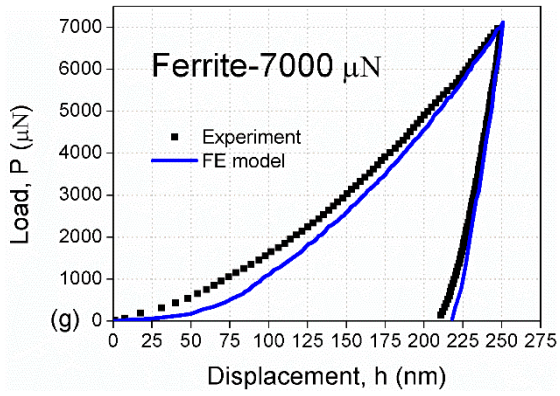
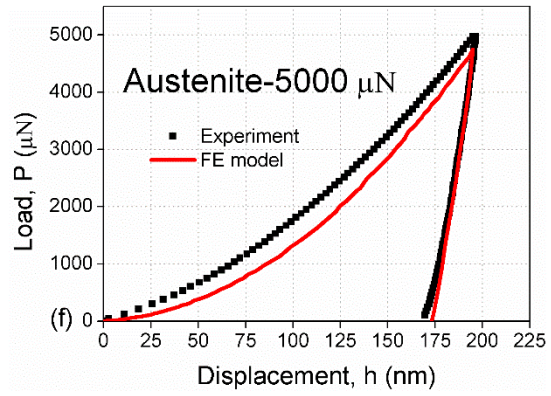


239

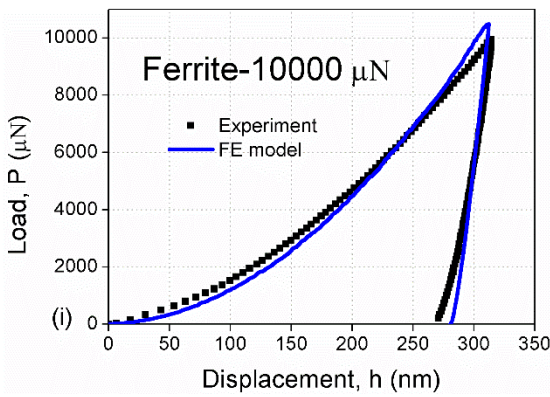
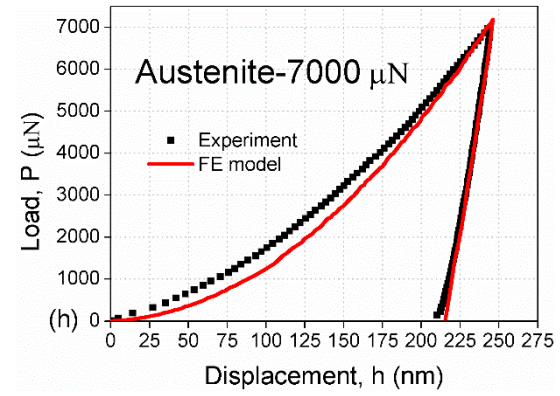




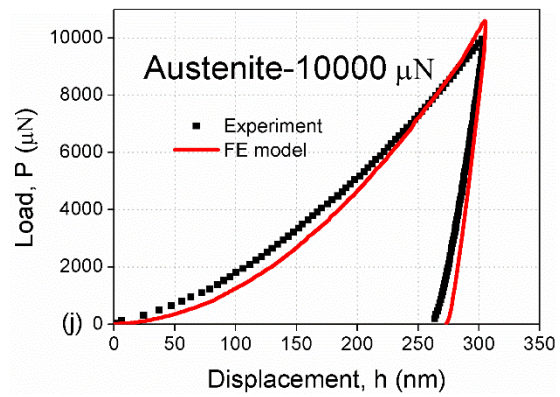
240



241



242

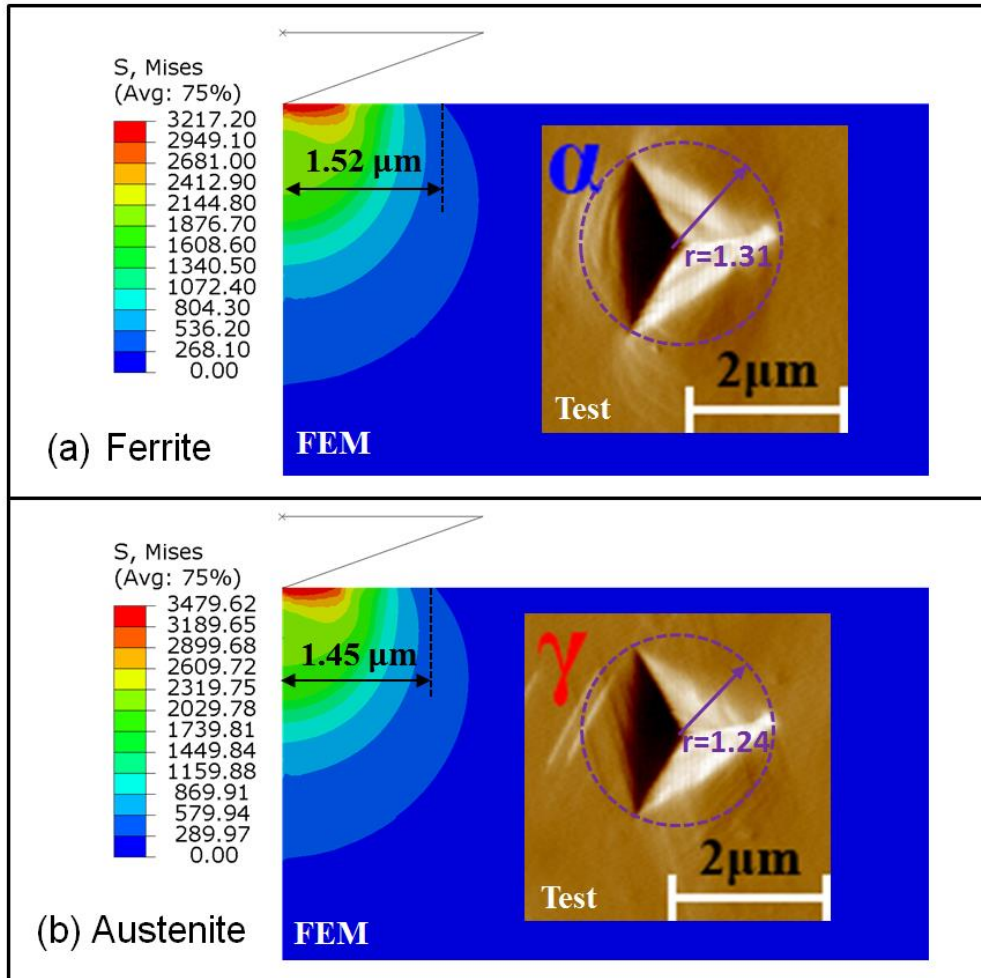


243

Fig. 7. Comparisons of load-displacement curves between experimental data and numerically predicted results of DSS 2205 (ferrite and austenite).

244

245



246

247

Fig. 8. Comparisons between FEM contour plots and scanning morphologies of experimental tests of (a) ferrite and (b) austenite in DSS 2205 under 5000 μN .

248

249

250

Table 4. Errors of SS 316L between experimental data and FE simulation results.

| Load, P_{max} (μN) | Error |
|--|---------|
| 1000 | -28.10% |
| 3000 | -9.17% |
| 5000 | -2.81% |
| 7000 | 0.03% |
| 10000 | 1.92% |

251

*Note: $\text{Error} = ((P_{\text{Test}} - P_{\text{FEM}}) / P_{\text{Test}}) \times 100\%$

252

Table 5. Errors of DSS 2205 between experimental data and FE simulation results.

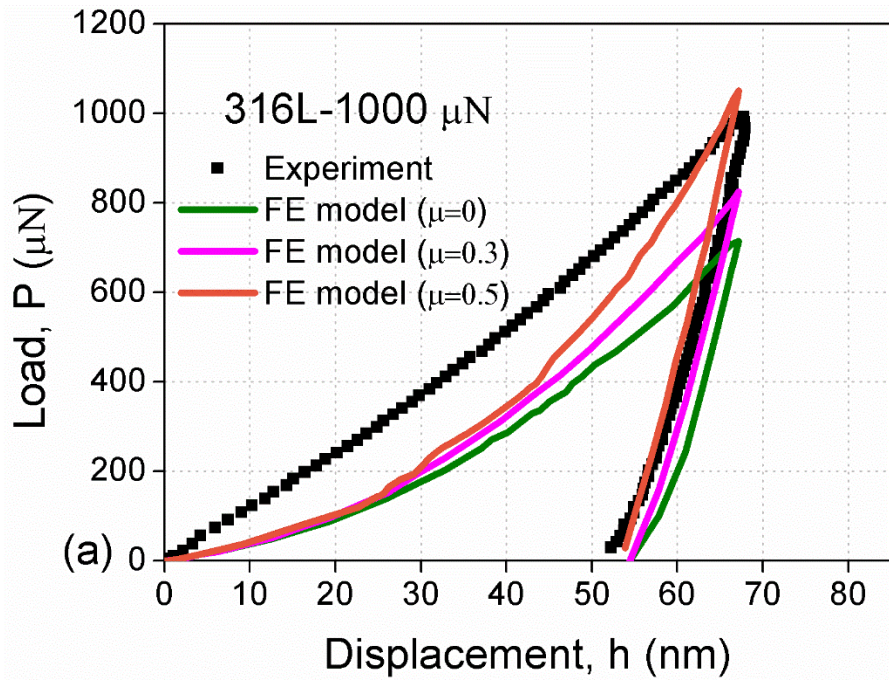
| Load, P_{\max} (μN) | Error | |
|------------------------------------|---------|-----------|
| | Ferrite | Austenite |
| 1000 | -8.91% | -12.71% |
| 3000 | -2.11% | -2.47% |
| 5000 | -2.91 | -4.52% |
| 7000 | 2.31% | 3.17% |
| 10000 | 4.78% | 5.31% |

253 *Note: $\text{Error} = ((P_{\text{Test}} - P_{\text{FEM}}) / P_{\text{Test}}) \times 100\%$

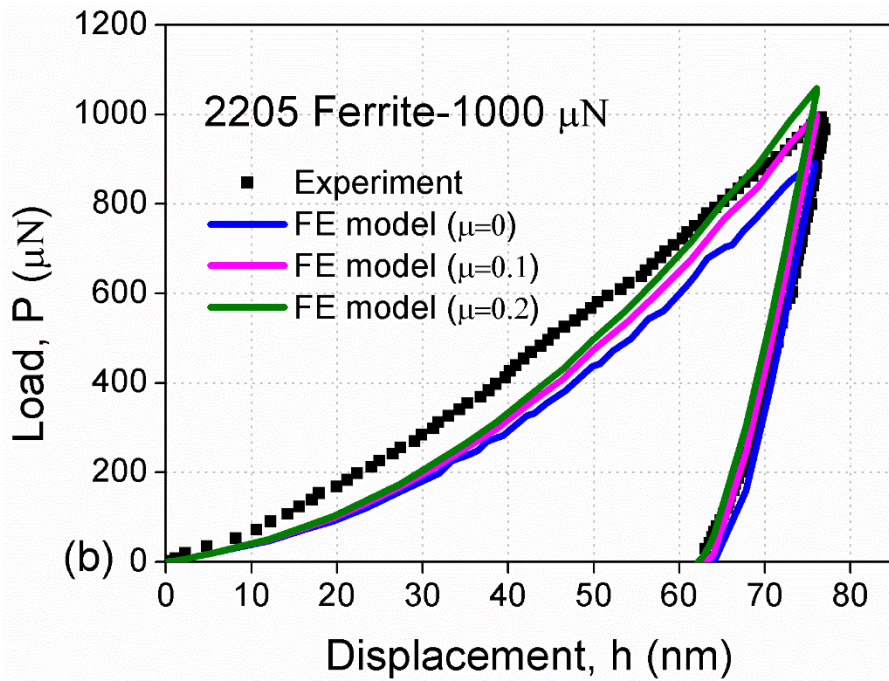
254

255 However, it is also seen that the errors of numerically predicted results and
 256 experimental tests of 316L and 2205 (ferrite and austenite) for the load of 1000 μN are -
 257 28.10%, -8.91% and -12.71%, respectively. One possible explanation is that the interactive
 258 friction between indenter and specimen has a more significant effect at lower indentation
 259 loads, so that the frictionless assumption is no longer valid. The numerically predicted
 260 results under 1000 μN case with different friction coefficients are presented in **Fig. 9**. It
 261 is seen that the errors between experiment and modeling decrease with increasing friction
 262 coefficient. However, it should be noted that, at a very low indentation depth, the testing
 263 results are sensitive to numerous other factors, such as sample surface roughness [28, 29],
 264 indenter tip radius [30, 31], substrate effects [7] and a uniqueness problem [8, 9].

265



266



267

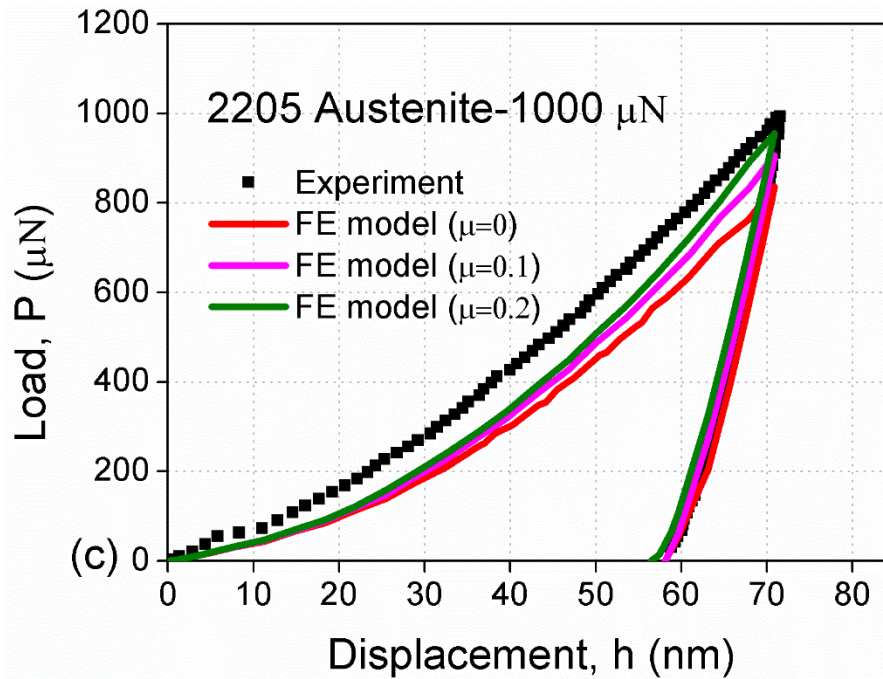


Fig. 9. Comparisons of load-displacement curves between experimental data and numerically predicted results with varied friction coefficient values under 1000 μN .

4. Conclusions

The main conclusions drawn from this work are as follows:

- Nano-indentation tests were employed on both single-phase (316L austenitic stainless steel) and dual-phase (2205 duplex stainless steel) materials. The measured values of nano-hardness, based on the Oliver-Pharr method for 316L and 2205, were found to decrease with increasing indentation depth, consistent with the nano-indentation size effect.
- An analytical model for representative yield strength (σ_y^R) with consideration of nano-indentation size effect was presented. With incorporation of densities of geometrically necessary dislocations and statistically stored dislocations, a functional expression is derived for dependence on indentation depth, expressed

283 as: $\sigma_y^R = H_0/\kappa + M\alpha Gb\sqrt{\frac{3}{2bh}}\tan^2\theta$.

284 • Two-dimensional finite element modeling results, within a power-law hardening
285 plasticity model, incorporating the load-dependent representative yield strength,
286 are thus able to reproduce the load-displacement curves to about 5% error
287 (compared to about 50% error previously) for nano-indentation test in the load
288 range from 3000 μN to 10000 μN . For lower loads, such as 1000 μN case, it is
289 shown that friction coefficient between indenter and specimen is a possible
290 important factor. With increasing friction coefficient, the numerical prediction
291 results became more consistent with experiments.

292 It should be noted that, once the indentation depth reaches the nanometer scale, the
293 tests are affected by additional factors, resulting in further dispersion of measured results.
294 Based on the analyses of 316L and 2205 stainless steels in this study, the prediction results
295 are in general agreement with experimental data for micro-scale tests, showing a suitable
296 predictive ability for reproducing nano-indentation curves.

297

298 **Acknowledgements**

299 The work is supported by the Innovation Project for Postgraduate Research & Practice
300 Innovation Program of Jiangsu Province (KYCX18_1093). We also gratefully
301 acknowledge the support from China Scholarship Council (CSC) and National University
302 of Ireland (NUI), Galway. This work has also been partly funded with the financial support
303 of Science Foundation Ireland as part of the MECHANICS joint project between NUI
304 Galway and University of Limerick under grant number of SFI/14/IA/2604 and the I-Form
305 Advanced Manufacturing Research Centre under grant number SFI/16/RC/3872.

306

307

- [1] A.A. Elmustafa, D.S. Stone. Nanoindentation and the indentation size effect: Kinetics of deformation and strain gradient plasticity. *Journal of the Mechanics and Physics of Solids*, 2003, 51(2): 357-381.
- [2] R. Rodriguez, I. Gutierrez. Correlation between nanoindentation and tensile properties: influence of the indentation size effect. *Materials Science and Engineering: A*, 2003, 361(1-2): 377-384.
- [3] Y.V. Milman, A.A. Golubenko, S.N. Dub. Indentation size effect in nanohardness. *Acta materialia*, 2011, 59(20): 7480-7487.
- [4] Z.S. Ma, S.G. Long, Y. Pan, Y.C. Zhou. Indentation depth dependence of the mechanical strength of Ni films. *Journal of Applied Physics*, 2008, 103(4): 043512.
- [5] Z.S. Ma, S.G. Long, Y. Pan, Y.C. Zhou. Loading rate sensitivity of nanoindentation creep in polycrystalline Ni films. *Journal of materials science*, 2008, 43(17): 5952-5955.
- [6] Z.S. Ma, S.G. Long, Y.C. Zhou, Y. Pan. Indentation scale dependence of tip-in creep behavior in Ni thin films. *Scripta Materialia*, 2008, 59(2): 195-198.
- [7] Z.S. Ma, Y.C. Zhou, S.G. Long, C. Lu. On the intrinsic hardness of a metallic film/substrate system: Indentation size and substrate effects. *International journal of plasticity*, 2012, 34: 1-11.
- [8] Z.S. Ma, Y.C. Zhou, S.G. Long, X.L. Zhong, C. Lu. Characterization of stress-strain relationships of elastoplastic materials: An improved method with conical and pyramidal indenters. *Mechanics of Materials*, 2012, 54: 113-123.
- [9] Z.S. Ma, Y.C. Zhou, S.G. Long, C.S. Lu. An inverse approach for extracting elastic-plastic properties of thin films from small scale sharp indentation. *Journal of Materials Science & Technology*, 2012, 28(7): 626-635.
- [10] J.W. Hutchinson, N. Fleck. Strain gradient plasticity. *Advances in applied mechanics*, 1997, 33: 295-361.
- [11] N.A. Fleck, G.M. Muller, M.F. Ashby, J.W. Hutchinson. Strain gradient plasticity: theory and experiment. *Acta Metallurgica et materialia*, 1994, 42(2): 475-487.

- [12] A. Ma, F. Roters, D. Raabe. A dislocation density based constitutive model for crystal plasticity FEM including geometrically necessary dislocations. *Acta Materialia*, 2006, 54(8): 2169-2179.
- [13] R.K. Abu Al-Rub, A.N.M. Faruk. Dislocation-based model for predicting size-scale effects on the micro and nano indentation hardness of metallic materials. *International Journal of Materials and Structural Integrity*, 2010, 4(2-4): 251-277.
- [14] M. Dao, N.V. Chollacoop, K.J. Van Vliet, T.A. Venkatesh, S. Suresh. Computational modeling of the forward and reverse problems in instrumented sharp indentation. *Acta materialia*, 2001, 49(19): 3899-3918.
- [15] N. Ogasawara, N. Chiba, X. Chen. Representative strain of indentation analysis. *J Mater Res*, 2005, 20(8): 2225-2234.
- [16] M. Zhao, N. Ogasawara, N. Chiba, X. Chen. A new approach to measure the elastic-plastic properties of bulk materials using spherical indentation. *Acta Materialia*, 2006, 54(1): 23-32.
- [17] N. Ogasawara, N. Chiba, X. Chen. Representative strain of indentation analysis. *J Mater Res*, 2005;20(8):2225-34.
- [18] M.F. Giordana, I. Alvarez-Armas, A. Armas. Microstructural characterization of EUROFER 97 during low-cycle fatigue. *J Nucl Mater*, 2012.
- [19] R.A. Barrett, P.E. O'Donoghue, S.B. Leen. A physically-based high temperature yield strength model for 9Cr steels. *Mat Sci Eng A*, 2018.
- [20] W.D. Nix, H. Gao. Indentation size effects in crystalline materials: a law for strain gradient plasticity. *Journal of the Mechanics and Physics of Solids*, 1998, 46(3): 411-425.
- [21] A. Bolshakov, G.M. Pharr. Influences of pileup on the measurement of mechanical properties by load and depth sensing indentation techniques. *Journal of materials research*, 1998, 13(4): 1049-1058.
- [22] A. Karimzadeh, M.R. Ayatollahi, M. Alizadeh. Finite element simulation of nano-indentation experiment on aluminum 1100. *Computational Materials Science*, 2014, 81: 595-600.
- [23] W.C. Oliver, G.M. Pharr. An improved technique for determining hardness and elastic modulus using load and displacement sensing indentation experiments. *J Mater*

Res1992;7(6):1564–83.

- [24] W.C. Oliver, G.M. Pharr. Measurement of hardness and elastic modulus by instrumented indentation: advances in understanding and refinements to methodology. *J Mater Res* 2004;19(1):3–20.
- [25] P. Tao, J.M Gong, Y.F. Wang, Y. Jiang, Y. Li, W.W. Cen. Characterization on stress-strain behavior of ferrite and austenite in a 2205 duplex stainless steel based on nanoindentation and finite element method. *Results in Physics*, 2018, 11: 377-384.
- [26] A. Basa, A. Barnoush, C. Thaulow. Nanomechanical testing of hydrogen effects on super duplex stainless steel. *Mechanical Testing and Diagnosis*, 2012, 2(2): 5.
- [27] N. Kheradmand, R. Johnsen, J.S. Olsen, A. Barnoush. Effect of hydrogen on the hardness of different phases in super duplex stainless steel. *International Journal of Hydrogen Energy*, 2016, 41(1): 704-712.
- [28] C. Walter, T. Antretter, R. Daniel, C. Mitterer. Finite element simulation of the effect of surface roughness on nanoindentation of thin films with spherical indenters. *Surface and coatings technology*, 2007, 202(4-7): 1103-1107.
- [29] A.C. Campbell, V. Buršíková, J. Martinek, P. Klapetek. Modeling the influence of roughness on nanoindentation data using finite element analysis. *International journal of mechanical sciences*, 2019, 161: 105015.
- [30] K.D. Bouzakis, N. Michailidis, S. Hadjiyiannis, G. Skordaris, G. Erkens. The effect of specimen roughness and indenter tip geometry on the determination accuracy of thin hard coatings stress–strain laws by nanoindentation. *Materials characterization*, 2002, 49(2): 149-156.
- [31] N. Yu, A.A. Polycarpou, T.F. Conry. Tip-radius effect in finite element modeling of sub-50 nm shallow nanoindentation. *Thin solid films*, 2004, 450(2): 295-303.